

PAPER

Development of a semi-empirical potential for simulation of Ni solute segregation into grain boundaries in Ag

To cite this article: Zhiliang Pan *et al* 2018 *Modelling Simul. Mater. Sci. Eng.* **26** 075004

View the [article online](#) for updates and enhancements.



IOP | ebooks™

Bringing you innovative digital publishing with leading voices to create your essential collection of books in STEM research.

Start exploring the collection - download the first chapter of every title for free.

Development of a semi-empirical potential for simulation of Ni solute segregation into grain boundaries in Ag

Zhiliang Pan¹ , Valery Borovikov², Mikhail I Mendeleev^{2,4} and Frederic Sansoz^{1,3,4} 

¹ Department of Mechanical Engineering, The University of Vermont, Burlington, VT 05405, United States of America

² Division of Materials Science and Engineering, Ames Laboratory, Ames, IA 50011, United States of America

³ Materials Science Program, The University of Vermont, Burlington, VT 05405, United States of America

E-mail: frederic.sansoz@uvm.edu and mendelev@ameslab.gov

Received 7 June 2018, revised 27 August 2018

Accepted for publication 4 September 2018

Published 18 September 2018



CrossMark

Abstract

An Ag–Ni semi-empirical potential was developed to simulate the segregation of Ni solutes at Ag grain boundaries (GBs). The potential combines a new Ag potential fitted to correctly reproduce the stable and unstable stacking fault energies in this metal and the existing Ni potential from Mendeleev *et al* (2012 *Phil. Mag.* **92** 4454–69). The Ag–Ni cross potential functions were fitted to *ab initio* data on the liquid structure of the Ag₈₀Ni₂₀ alloy to properly incorporate the Ag–Ni interaction at small atomic separations, and to the Ni segregation energies at different sites within a high-energy $\Sigma 9$ (221) symmetric tilt GB. By deploying this potential with hybrid Monte Carlo/molecular dynamics simulations, it was found that heterogeneous segregation and clustering of Ni atoms at GBs and twin boundary defects occur at low Ni concentrations, 1 and 2 at%. This behavior is profoundly different from the homogeneous interfacial dispersion generally observed for the Cu segregation in Ag. A GB transformation to amorphous intergranular films was found to prevail at higher Ni concentrations (10 at%). The developed potential opens new opportunities for studying the selective segregation behavior of Ni solutes in interface-hardened Ag metals and its effect on plasticity.

Supplementary material for this article is available [online](#)

⁴ Authors to whom any correspondence should be addressed.

Keywords: semi-empirical interatomic potential, stacking fault energy, grain boundary segregation, Ag–Ni alloy

(Some figures may appear in colour only in the online journal)

1. Introduction

Grain boundary (GB) segregation refers to the local enrichment of solute atoms at GBs in polycrystalline materials [1]. It has long been observed that solute segregation can adversely reduce the ductility and fracture toughness of metallic alloys through GB embrittlement [2–5]. By contrast, it was recently discovered that GB segregation can increase the strength of nanocrystalline materials by suppressing grain growth [6, 7] and GB sliding [8] mechanisms, thus offering a new approach to engineer unprecedentedly strong and tough bulk metallic nanostructures [9]. Also, at high concentrations, solute segregation can induce structural transitions at GBs [10] leading to the formation of different types of interfacial phases, such as GB complexions [11], which are considered to be important in materials design [12, 13].

GB segregation and its effects on material properties have been extensively investigated through both experimental [8, 14, 15] and atomistic simulation methods [16–18]. Atomistic simulations have enabled high-fidelity GB segregation studies that could provide insight not available even from the most advanced experimental characterization techniques, such as high-resolution transmission electron microscopy and atom probe tomography. For example, atomistic simulations revealed that change in a Cu $\Sigma 5$ (310) GB from single to split kite structural units is responsible for the abnormal Ag segregation in this type of boundary [19], whereas capturing such subtle structural transitions experimentally remains challenging. *Ab initio* calculations often used to simulate complex atomic interactions in metals are limited to small systems containing less than a few thousand atoms. This makes them not suitable for studying long-range phenomena by Monte Carlo (MC), molecular dynamics (MD), or hybrid MC/MD simulations [10, 20, 21], which usually involves using several millions of atoms and large numbers of time steps to maintain stable statistics in calculating solute concentrations near both chemical and structural equilibrium conditions. Therefore, these simulations require semi-empirical interatomic potentials, and their outcomes heavily depend on the ability of the employed potential to predict the desired properties.

GB segregation tends to occur in immiscible metallic alloys [22] where solutes have a very limited solubility in the matrix. Some examples include Cu–Ag [23], Cu–Zr [24], Cu–Ta [25], Cu–Nb [26], and Ni–W [27], from which promising alloys with extraordinary mechanical properties have been created by taking advantage of the GB segregation. Semi-empirical potentials [28–31] have been developed for some of these alloys, and used to study how segregated solute atoms improve their properties. For example, in atomistic simulations using an angle-dependent interatomic potential [30] for Cu–Ta alloys, Frolov *et al* [22] showed that Ta atoms segregated into GBs could suppress grain growth in nanocrystalline Cu and, meanwhile, increase its strength. With a potential developed for Cu–Zr [29], a common alloy system involved in making bulk metallic glasses, Pan and Rupert [10] studied the roles of Zr segregation on disordering transitions in Cu GBs, which resulted in the finding that amorphous intergranular films could potentially enhance the ductility without sacrificing strength in nanocrystalline materials [32, 33]. Using a slightly modified version of this semi-empirical potential, Borovikov *et al* showed that these amorphous intergranular films have dramatic effects on dislocation nucleation processes from GBs [34].

The present study focuses on the Ag–Ni alloy because this alloy system is also immiscible [35] and consists of two important metals. Ag is known to have the highest room-temperature electrical conductivity, but also exhibits relatively low strength. The former property makes Ag ideal as conductive material in electronic and optoelectronic applications, but Ag interconnects can easily fail under extreme load and temperature conditions. Ni solute segregation could be a viable solution to help improve the strength of Ag metals, without sacrificing the electrical conductivity. However, while there are a few experimental studies [36, 37], no atomistic simulations have been conducted to understand solute segregation in Ag–Ni alloys because of the lack of a reliable and efficient interatomic potential.

In this article, we present a Finnis–Sinclair (FS) potential for Ag–Ni alloys suitable for simulations of GB segregation of Ni in Ag. The Ag–Ag interaction is modeled with a new potential fitted to correctly reproduce the liquid structure and the stable and unstable stacking fault energies in Ag, with a fitting database gleaned from *ab initio* calculations, while an existing potential from Mendeleev *et al* [38] is used to describe the Ni–Ni interaction. The cross potential functions used to describe the interaction between Ag and Ni atoms were also fitted to *ab initio* data on the Ag₈₀Ni₂₀ liquid structure, segregation energy of Ni at different sites of the $\Sigma 9$ (221) symmetric tilt GB in Ag, and dipole formation energy of Ni in both single crystal and $\Sigma 9$ (221) GB in Ag. This potential is shown to reproduce with high precision not only properties at 0 K temperature included in the potential fitting, but also those at elevated temperature. The potential is tested and applied to the study of Ni solute segregation in three types of Ag GBs at 500 K with different Ni concentrations using hybrid MC/MD simulations. The developed potential is available in the supplementary material, which is available online at stacks.iop.org/MSMS/26/075004/mmedia, and in the Interatomic Potentials Repository maintained by the National Institute of Standards and Technology (www.ctcms.nist.gov/potentials) [39].

2. Computational methods

The potential fitting database was obtained from the *ab initio* calculations performed using the Vienna *ab initio* simulation package implemented based on the Kohn–Sham density functional theory [40]. Three types of calculations were performed: wavefunction optimization to calculate the total energy of a specific atomic configuration, geometry optimization to calculate the local minimum potential energy of a system, and MD to track the trajectory of temporal system evolution, with an integration time step of 2 fs. In all three cases, plane wave basis set was used to expand the Kohn–Sham orbitals with an energy cutoff of 350 eV. The exchange-correlation functional was developed by Perdew, Burke, and Ernzerhof (PBE) [41] in a form of generalized gradient approximation [42]. The interaction between ions was described with projector augmented-wave method potentials [43, 44]. Since large simulation cells were used, only Γ point calculation was performed for wavefunction optimization, which was assumed to converge when the total energy difference between the last two iterations was less than 1×10^{-6} eV. Convergence for geometry optimization was considered when the maximum force acting on the atoms reached less than 1×10^{-4} eV \AA^{-1} .

The performance of the developed FS potential was tested using hybrid MC/MD simulations implemented in the Large-scale Atomic/Molecular Massively Parallel Simulator code [45]. All MC/MD simulations were performed at 500 K, using an integration time step of 1 fs for the MD steps. The total energy of each pure Ag system was first minimized by conjugate gradient method. Then, the system was further relaxed with a Nose–Hoover thermostat and a Parrinello–Rahman barostat for 10 ps under zero pressure at 500 K. The doping process was carried out by the MC method in a variance-constrained semigrand

Table 1. Stable and unstable stacking fault energies of pure Ag calculated with different interatomic potentials.

Potential	γ_{SF} (meV \AA^{-2})	γ_{USF} (meV \AA^{-2})
Mishin [28]	1.11	7.15
Wu [56]	1.11	7.15
Zhou [57]	0.37	5.61
Adams [58]	0.09	7.41
Ackland [59]	1.41	13.22
Sheng [60]	1.80	6.95
This work	1.74	6.20

canonical ensemble [46] after every 100 MD steps, with the target global composition achieved by adjusting the initial chemical potential difference during the simulation [20]. The convergence was confirmed when the fitted slope of the system potential energy over the last 2000 MC steps was found less than 0.001 eV/step. The adaptive common neighbor analysis [47, 48] was used to identify the structural environment of each atom. In the following, Ag fcc atoms are colored in green, hexagonal close-packed ones are colored in red, and all other atoms are colored in white, unless otherwise specified. All Ni atoms are colored in dark blue. Atomistic snapshots were made using the open-source visualization tool (OVITO) [49].

3. Semi-empirical potential development

The FS formalism [50] was used to describe the atomic interactions. The total potential energy U of a system containing N atoms is given by

$$U = \sum_{i=1}^{N-1} \sum_{j=i+1}^N \varphi^{\alpha_i \alpha_j}(r_{ij}) + \sum_{i=1}^N \Phi^{\alpha_i}(\rho_i). \quad (1)$$

Here, the subscripts i and j are atom indices, r_{ij} is the separation distance between atoms i and j , ρ_i is the background charge density given by

$$\rho_i = \sum_j \Psi^{\alpha_i \alpha_j}(r_{ij}), \quad (2)$$

and α_i is the element type of atom i . For the Ag–Ni binary alloy, α_i is either Ag or Ni. A total of eight functions are needed for this potential: φ^{AgAg} , Φ^{Ag} and Ψ^{AgAg} obtained by fitting to the properties of pure Ag, φ^{NiNi} , Φ^{Ni} and Ψ^{NiNi} obtained by fitting those of pure Ni, and two cross functions, φ^{AgNi} and Ψ^{AgNi} should be fitted to Ag–Ni alloy properties.

3.1. Pure Ag potential

Semi-empirical potentials cannot perfectly reproduce all materials properties with accuracy. However, they can be optimized to reproduce main properties of interest. In this work, special focus was on developing a potential to simulate Ni segregation in Ag GBs, as well as, the dislocation processes and plastic deformation behavior in Ag affected by Ni solute segregation. For the latter, the stable and unstable stacking fault energies were considered important parameters to match. Specifically, it has been established that the stresses required for partial dislocation nucleation in fcc metals are linearly related to the unstable stacking fault energy [51–55]. For pure Ag, table 1 lists the stacking fault energies predicted using

Table 2. Stable and unstable stacking fault energies of pure Ag predicted from *ab initio* calculations or measured from experimental work in the literature.

References	γ_{SF} (meV \AA^{-2})	γ_{USF} (meV \AA^{-2})	Remark
Jin <i>et al</i> [61]	1.00	5.68	<i>Ab initio</i>
Wu <i>et al</i> [62]	1.06	6.93	<i>Ab initio</i>
Li <i>et al</i> [63]	1.06	7.49	<i>Ab initio</i>
Li <i>et al</i> [64]	1.08		<i>Ab initio</i>
Kibey <i>et al</i> [65]	1.12	8.30	<i>Ab initio</i>
Suzuki <i>et al</i> [66]	1.31		Experiment
Tian <i>et al</i> [67]	1.37		<i>Ab initio</i>
Hartford <i>et al</i> [68]	1.81		<i>Ab initio</i>
Rosengaard <i>et al</i> [69]	2.12		<i>Ab initio</i>
Schweizer <i>et al</i> [70]	2.37		<i>Ab initio</i>
Kioussis <i>et al</i> [71]	3.12	11.86	<i>Ab initio</i>
This work	1.74	6.20	<i>Ab initio</i>

several potentials from the existing literature [28, 56–60]. This table reveals clear inconsistency across these potentials. Table 2 summarizes literature values of stacking fault energy either predicted from *ab initio* calculations or measured from experiments [61–71]. This table also shows that the maximum predicted value is more than three times larger than the minimum one, suggesting a large discrepancy for the reference values in Ag as well. The conflicting predictions from *ab initio* might be attributed to the fact that different atomic configurations and implementations of density functional theory were used to perform the calculations. The atomic configurations used in the calculations included slab models formed by numbers of (111) atomic layers plus two (111) free surfaces [62, 68], supercells containing two twins to produce two identical stacking faults under periodic boundary conditions [63], and supercells to produce only one stacking fault by removing one (111) atomic layer [64, 67, 70]. The implementations of density functional theory used in the calculations differed in the exchange-correlation functional, whether full-potential method or frozen-core approximation were used, the types of pseudopotentials used in the frozen-core approximation, etc. Therefore, the calculation errors might come from various sources. For example, calculation error will be introduced if insufficient number of the atomic layers is used in the slab model [62]. The linear-muffin-tin-orbital method within atomic-sphere approximation can overestimate the stacking fault energy by a factor of two when compared with the result by a pseudopotential approach within the local density approximation [70]. Early *ab initio* calculations used small supercells and calculated the stacking fault energy based on the assumption ‘that the stacking fault energy is determined by covalent bonds between the hexagonal planes produced by s–d hybridization’ [70] and that fault interactions are short ranged [68] since free electrons will be localized around the stacking fault by forming covalent bonds. However, Ag has less s–d hybridization, meaning that some free electrons will not localize, but rather tend to interact with free electrons within a longer range [68, 70]. This breaks the short-range assumption and leads to smaller accuracy when the simulation cell is too small, which is usually the case for these early *ab initio* calculations.

To address this issue, we have performed *ab initio* calculations using a slab model in a much larger simulation cell, as shown in figure 1. This cell contained 18 (111) atomic layers and 864 atoms. The configurations of unstable and stable stacking faults were created by shifting the upper part of the single crystal by a distance of $a_0/2\sqrt{6}$ and $a_0/\sqrt{6}$ in the $[11\bar{2}]$ direction, respectively, where a_0 is the lattice constant of Ag. The stacking fault energy was

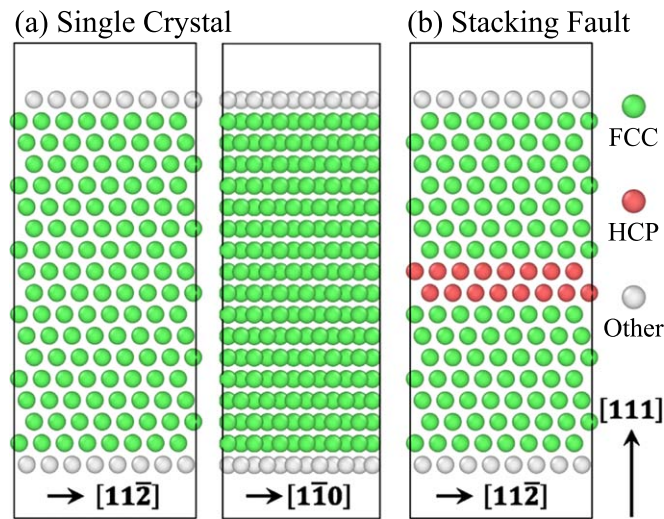


Figure 1. Atomistic models used for large-scale *ab initio* calculations of (a) single crystal and (b) stacking-faulted configurations used to compute the stacking fault energy.

calculated as the energy difference per cross-section area between the single crystal and faulted configurations after geometry relaxation. The values obtained in this work are given in table 2. To test if this supercell is large enough, we also calculated the stacking fault energy using a smaller cell containing 12 (111) atomic layers and 576 Ag atoms. The result is consistent with the large cell, with a relative error of only about 0.06%, indicating that the number of the atomic layers and atoms in the supercell is sufficient to reliably calculate the stacking fault energy.

The comparison of data presented in tables 1 and 2 shows that no existing semi-empirical potential is capable of reproducing the values of both stable and unstable stacking fault energies obtained in the present study from *ab initio* calculations. This warranted the need for developing a new potential for pure Ag. The target property values used for the fitting of the new Ag potential were obtained from either our *ab initio* calculations or the literature [28, 72] (see table 3).

It should be mentioned that the *ab initio* calculations with PBE functional overestimate the lattice parameter for the fcc Ag, giving $a_0 = 4.1608 \text{ \AA}$, in contrast to the well-accepted value of $a_0 = 4.09 \text{ \AA}$. To take this effect into account, it has been suggested that interatomic distances from *ab initio* calculations should be re-scaled by a factor of $4.09/4.1608$ before the fitting process [28]. This approach may work well for a potential development for a single component system. However, in the case of binary alloys, it may actually introduce an additional challenge for using the *ab initio* data on the liquid structure. The point is that the *ab initio* calculations with PBE functional do give a good prediction for fcc Ni lattice parameter ($a_0 = 3.5165 \text{ \AA}$). Since the same rescaling factor should be applied to the entire simulation cell it may fix the problem with the Ag–Ag separations but make unrealistic the Ag–Ni and Ni–Ni separations. Therefore, in order to use the *ab initio* data on the liquid structure (see below) we preferred to develop a potential which is completely consistent with the *ab initio* data and therefore, used the *ab initio* Ag lattice parameter which is quoted in table 3 as the target value.

Table 3. Target values of bulk properties of pure Ag obtained with *ab initio* calculations and the values reproduced with this potential. For target values, we used: * this work, \$ [28], and & [72].

Property		Target value	FS potential
Lattice constant (Å)	a_0 (fcc)	4.16*	4.16
Cohesive energy (eV/atom)	E_{coh} (fcc)	2.85\$	2.97
Elastic constant (GPa)	C_{11}	124\$	123
	C_{12}	93.4\$	94
	C_{44}	46.1\$	47
Vacancy formation and migration energy (eV/atom)	E_f^V (unrelaxed fcc)		1.16
	E_f^V (relaxed fcc)	1.1\$	1.14
	E_m^V (fcc)	0.66\$	0.65
Interstitial formation energy (eV/atom)	E_f^i ($\langle 100 \rangle$ fcc)		2.66
Cohesive energy difference (eV/atom)	$\Delta E_{\text{fcc} \rightarrow \text{bcc}}$	0.039\$	0.036
	$\Delta E_{\text{fcc} \rightarrow \text{hcp}}$	0.003\$	0.006
Surface energy (meV Å ⁻²)	γ_{100} (fcc at $T = 0$ K)	71\$	52
Stacking fault energy (meV Å ⁻²)	γ_{SF} (fcc at $T = 0$ K)	1.74*	1.69
	γ_{USF} (fcc at $T = 0$ K)	6.20*	6.46
	T_m (fcc)	1234&	1209
Enthalpy of fusion (eV/atom)	ΔH_m (fcc, T_m)	0.117&	0.112
Change in volume upon melting (%)	$\Delta V_m / V_s$ (fcc, T_m)		5.1

It is worth noting that the atomic separations within crystalline interfaces may vary from those in single crystals. To accurately reproduce the interactions at all atomic separations, we included a liquid structure in the fitting process by adjusting the potential parameters so that the pair correlation function of a liquid structure described with this potential is consistent with that of an input liquid structure. For pure Ag, the latter was generated by running *ab initio* MD in a cubic simulation cell containing 250 Ag atoms at 1100 K in a canonical (NVT) ensemble. The volume of the simulation cell was chosen as to achieve an average pressure close to zero after a duration of 20 ps. The pair correlation function of the liquid structure resulting from a 20 ps simulation is shown in figure 2.

The newly developed pair function φ^{AgAg} , embedded function Φ^{Ag} , and electron density function Ψ^{AgAg} are shown in figure 3. Table 3 indicates that this potential reproduces most bulk properties and stacking fault energies included in the fitting process with a good accuracy. In addition, the liquid structure predicted from the potential is perfectly consistent with the structure obtained from our *ab initio* MD, as shown in figure 2. To test the potential, we calculated the generalized stacking fault (GSF) energy curve, which is important for dislocation-assisted plastic deformation mechanisms [73]. Following the methodology in the literature [74], figure 4 presents the unrelaxed GSF energy curve calculated as the energy cost of rigidly shifting the upper part of the single crystal slab in the $[11\bar{2}]$ direction, and the

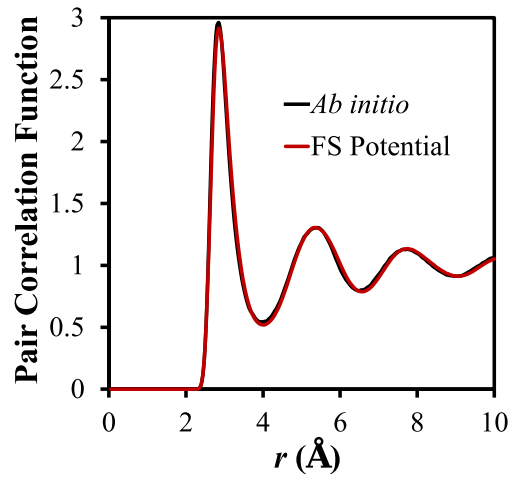


Figure 2. Pair correlation function of the pure Ag liquid at 1100 K.

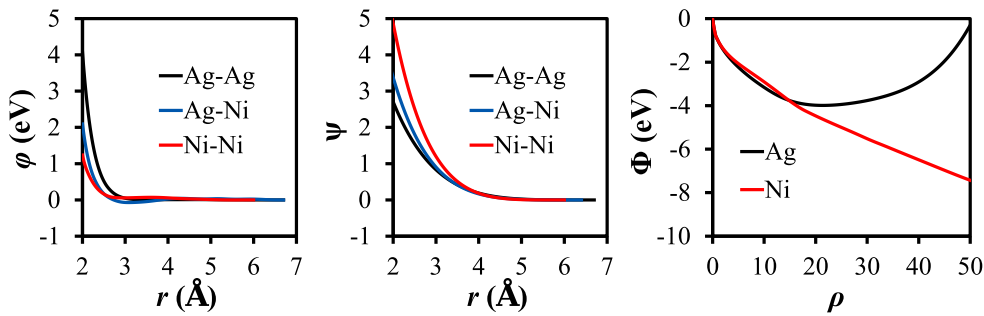


Figure 3. Potential functions of this Ag-Ni potential.

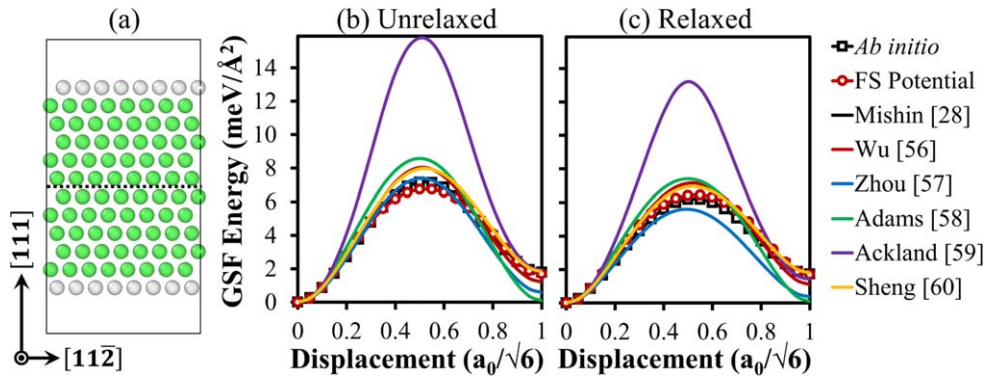


Figure 4. Generalized stacking-fault energy curves. Atomic configuration (a) used to calculate the unrelaxed (b) and relaxed (c) generalized stacking fault energy curves with *ab initio* calculation and this potential, as well as other potentials in the literature, where Mishin and Wu potentials give the same GSF curves. Our FS potential provides the best match to the *ab initio* data.

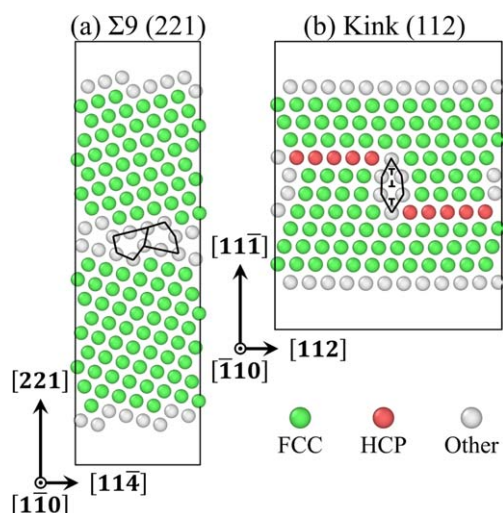


Figure 5. Structure of (a) $\Sigma 9$ (221) symmetric tilt GB and (b) kink (112) twin-boundary defect obtained with *ab initio* calculations.

relaxed one obtained by relaxing all atoms in the [111] direction. It is shown that the results with the developed FS potential agree very well with the *ab initio* data, whereas the potentials from the literature lead to significant differences.

Furthermore, $\Sigma 9$ GBs have been found to represent the highest fraction of all GBs in nanotwinned Cu, playing an important role in plastic deformation mechanisms [75]. Similar to Cu, Ag can also form abundant nanotwins easily due to its low stacking fault energy [76–78], suggesting that $\Sigma 9$ GBs may also be important for nanotwinned Ag. Past theoretical studies have shown a correlation between the equilibrium structure of the $\Sigma 9$ symmetric tilt GBs and the metal type: fcc metals with low stacking fault energy such as Cu tend to favor pure E structural units, whereas those with high stacking fault energy such as Al, favor CB structural units [79]. Figure 5(a) shows the equilibrium structure of a $\Sigma 9$ (221) symmetric $\langle 110 \rangle$ -tilt GB predicted in pure Ag from *ab initio* calculations. Consistent to the literature findings [80], only E structural units are present in this type of boundary. Likewise, our new potential, as well as six other potentials, predicts the same E structural units in this interface, although this structure was not directly included in the potential fitting process.

Moreover, the kink step defects attached to coherent twin boundaries are found to be pervasive in as-deposited nanotwinned Cu, and have proved to be important for understanding the plastic deformation mechanisms of nanotwinned fcc metals [81, 82]. Figure 5(b) shows the relaxed structure of a twin-boundary kink defect from *ab initio* calculations. The minimum kink height is equal to one periodic length in the [111] direction. Kink steps can be viewed as one small segment of an incoherent $\Sigma 3$ (112) twin boundary, containing three pure partial dislocations, as described in past atomistic studies [82]. Again, our new potential, as well as six other potentials, predicts the same structure in this kink despite the fact that it was not included in the potential fitting procedure.

Figure 6 displays the calculated energies for the $\Sigma 3$ (111) coherent twin boundary, $\Sigma 9$ (221) GB, and kink (112) defect. In our calculations, the kink energy is defined as the energy difference per unit kink area between the model with the kink (see figure 5(b)) and a similar model without kink, i.e. containing a perfect twin boundary. Because the stable stacking fault energy is included in the potential fitting, the twin boundary energy ($0.90 \text{ meV } \text{\AA}^{-2}$) is found

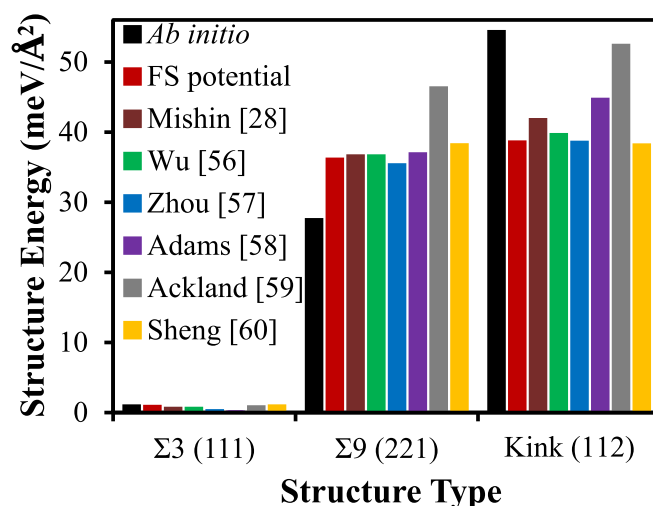


Figure 6. Structure-energy values for $\Sigma 3$ (111) (coherent twin boundary), $\Sigma 9$ (221), and kink (112) defects calculated with *ab initio*, the FS potential developed within the present study, and potentials in the literature.

very close to the *ab initio* value, which is about half of the stable stacking fault energy ($1.69 \text{ meV } \text{\AA}^{-2}$). The $\Sigma 9$ (221) GB and kink (112) energies were not included in the potential fitting. Nonetheless, the former still agrees well with the *ab initio* data, with somewhat better results than most predictions from other potentials. All potentials, however, underestimate the kink (112) defect energy predicted by *ab initio*. It is worth noting that these calculations used a larger simulation cell to ensure the stability of the kinks. In fact, four of the seven potentials tested could not achieve a stable kink structure when the simulation cell was as small as that used in the *ab initio* calculations. We attribute this discrepancy to local strains generated in the small simulation cell after relaxation to reduce excessive surface forces, as evidenced by the slightly curved top and bottom atomic layers shown in figure 5(b).

3.2. Ag–Ni cross potential

To fit the cross density function, we determined the difference between the cohesive and unrelaxed bi-vacancy formation energies for the AgNi B2 crystal phase from *ab initio* calculations. In the FS formalism, this quantity does not depend on pair potentials and can be used to normalize the cross density function. First, we determined the equilibrium lattice parameter and cohesive energy of the B2 phase (3.058 \AA and 3.360 eV , respectively). Then we constructed a $5 \times 5 \times 5 a_0^3$ B2 crystal configuration containing 125 Ag atoms and 125 Ni atoms and removed one Ag atom and one Ni atom located far away from each other. The bi-vacancy formation energy was calculated as $(E - 248E_0/250)/2 = 1.218 \text{ eV/atom}$, where E and E_0 are the total energies for the perfect crystal and bi-vacancy configurations, respectively. The difference between cohesive energy and bi-vacancy formation energy for AgNi B2 structure is thus $3.360 - 1.218 = 2.142 \text{ eV}$. The compound formation energy of AgNi B2 phase (0.302 eV/atom) was also used in the potential development procedure to provide a reasonable solution thermodynamics.

To properly incorporate the Ag–Ni interaction at small separations in transition states, the potential was fitted to the *ab initio* data on the liquid structure of the $\text{Ag}_{80}\text{Ni}_{20}$ alloy. The

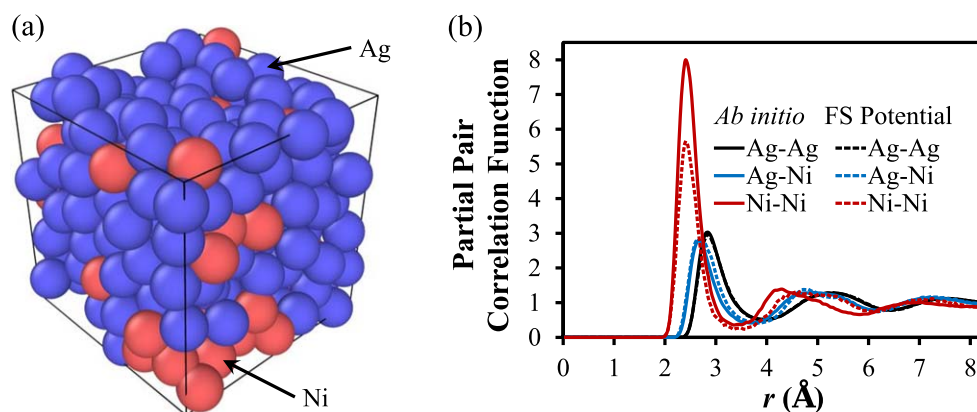


Figure 7. $\text{Ag}_{80}\text{Ni}_{20}$ liquid structure. (a) Atomic snapshot of $\text{Ag}_{80}\text{Ni}_{20}$ liquid at 1100 K after 20 ps of *ab initio* MD. (b) Comparison of partial pair correlation functions of this liquid from *ab initio* and the FS potential.

liquid structure was generated by running *ab initio* MD in a cubic simulation cell containing 200 Ag atoms and 50 Ni atoms at a temperature of 1100 K in a canonical (NVT) ensemble, with a cell volume chosen to reach near-zero average pressure during the simulations. The actual Ag–Ni alloy has positive deviations from ideality and decomposes into two liquid solutions at this temperature. However, the simulation cell was too small and the simulation time was too short to fully observe this phenomenon. Yet the Ni–Ni partial pair correlation function clearly indicates the tendency to the formation of Ni-rich clusters (see figure 7(a)).

In order to reproduce the liquid structure obtained from the *ab initio* MD simulation we used the method based on the Born–Green–Bogoliubov equation described in [83]. This equation, however, is derived for a homogeneous liquid, and thus the tendency for liquid decomposition poses a challenge. To overcome this issue, we always started from the first snapshot obtained from the *ab initio* MD simulation and run the classical MD simulation only 20 ps saving snapshots every 0.2 ps. These snapshots were used to produce a new version of the potential (along with the equations for other target properties used in the potential development procedure). Figure 7(b) shows that the developed FS potential provides a reasonable agreement with the liquid structure obtained from the *ab initio* MD simulation, although it somewhat underestimates the tendency for the Ni cluster formation. This does not necessarily mean that this potential will also provide the correct predictions for the decomposition in solid solutions; so, special caution should be exercised about this (see below). However, it should work well for dilute solutions because it does provide an excellent agreement with the Ag–Ni partial pair correlation function.

To fit the Ni segregation energy in Ag, segregation energies at different GB sites were obtained from the *ab initio* calculations. We chose the $\Sigma 9$ (221) symmetric tilt GB with a $\langle 110 \rangle$ tilt axis. Six possible segregation sites were considered within this GB, as shown in figure 8(a). Figure 8(b) shows the Ni segregation energies at these sites from first-principle calculations. The segregation energy at each site was calculated as the difference in substitutional energy between a GB and a perfect crystal of equivalent size. The GB substitutional energy at a specific site was defined as the total energy difference between the pure GB and the same boundary with one Ag atom at this site replaced by a Ni atom. Likewise, the

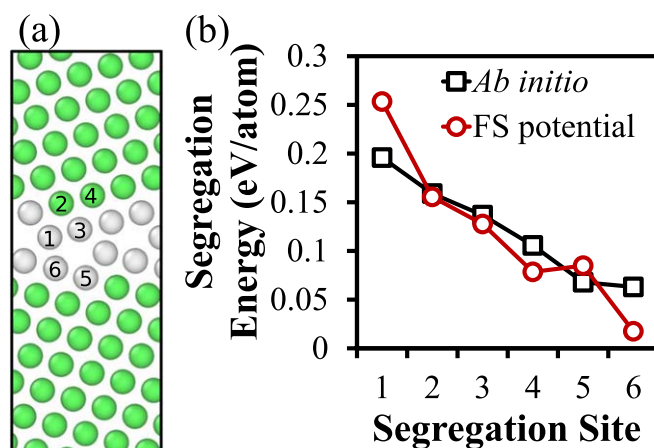


Figure 8. Segregation energies in a $\Sigma 9$ (221) symmetric tilt GB. (a) Six segregation sites in the $\Sigma 9$ (221) GB and (b) the Ni segregation energy at these sites calculated with *ab initio* and this potential.

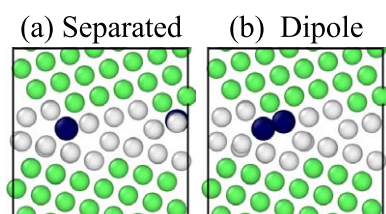


Figure 9. Ni dipole formation energy in the $\Sigma 9$ (221) GB. Atomic configurations with (a) two separated Ni atoms and (b) one Ni dipole.

Table 4. Dipole formation energy (eV) of Ni in Ag predicted from *ab initio* and this potential.

Structure	<i>Ab initio</i>	FS potential
Single crystal	0.1124	0.1039
$\Sigma 9$ (221) GB	0.0771	0.0549

single crystal substitutional energy was defined as the total energy difference between the pure single crystal and the single crystal with one Ag atom is replaced by a Ni atom.

When segregated into a crystalline interface, solute atoms may either distribute uniformly inside the boundary, leading to homogeneous segregation, or cluster, leading to heterogeneous segregation [84]. To correctly reproduce the situation for the Ni solutes in the chosen Ag GB, we included the Ni dipole formation energy in the potential development procedure. Figure 9 shows a close-up view on the two $\Sigma 9$ (221) GB configurations used for this calculation. One boundary contained two separated Ni atoms and the other one has a Ni dipole. The dipole formation energy was calculated as the total energy difference between the

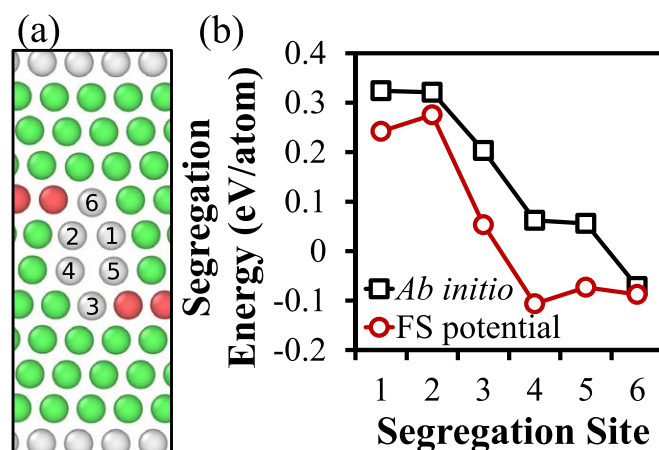


Figure 10. Segregation energies in a twin-boundary kink step defect. (a) Six segregation sites in the kink (112) defect and (b) the Ni segregation energy at these sites calculated with *ab initio* and this potential.

two configurations, with a positive value indicating a preference for dipole formation. The calculated dipole formation energy is provided in table 4. Since Ag and Ni are immiscible at low temperature, Ni atoms remain preferentially clustered inside Ag single crystals. Therefore, we have also included the Ni dipole formation energy in Ag single crystal, with the *ab initio* results provided in table 4 as well.

The final fitting for the cross potential functions of Ag–Ni are shown in figure 3, together with the functions for pure Ag and Ni. With this potential, the calculated difference between cohesive energy and bi-vacancy formation energy for AgNi B2 structure is equal to 1.984 eV/atom. The compound formation energy is found equal to 0.328 eV/atom. Both predictions agree with our *ab initio* data. The segregation energies of Ni at different sites in the $\Sigma 9$ (221) GB obtained with this potential is given in figure 8(b), together with the *ab initio* data, demonstrating that this potential reproduces the segregation energy very well. It is worth noting that the site with high segregation energy does not always reside inside the GB, but could also be a neighboring lattice site, e.g. site 2 in figure 8(b). This is consistent with past experimental observations that Ni atoms could be found to segregate into bulk planes adjacent to a GB [85]. The dipole formation energies of Ni in this GB and single crystal are also in agreement with our *ab initio* calculations (see table 4).

Furthermore, it was verified that the predicted Ni segregation energy at the kink (112) twin boundary structure shown in figure 5(b) agreed reasonably with *ab initio* data. An MD simulation study by Ke and Sansoz [16] showed that twin-boundary kink steps were preferential sites for segregation of Cu impurities in nanotwinned Ag. Substitutional Ni segregation energies at six different sites of a kink (112) structure are presented in figure 10. The segregation energy predicted with the developed FS potential agrees well with the *ab initio* data for sites 1 and 2 that have highest segregation energies over other sites, despite not being included in the potential development procedure. It thus indicates that this potential could be suitable for simulation of the Ni segregation behavior at kink defects inside twin boundaries, in addition to GB segregation, making this potential ideal for the study of Ni segregation in nanotwinned Ag.

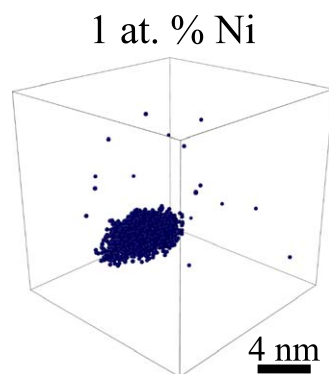


Figure 11. Ni cluster formed in an Ag single crystal with a solute concentration of 1 at% Ni at a temperature of 500 K. All Ag atoms are removed to help visualize the Ni cluster.

4. Applications of the new potential

4.1. Clustering segregation behavior with low Ni contents

Figure 11 shows the equilibrated 1 at% Ni atom distribution in Ag single crystal obtained in hybrid MC/MD simulation. The simulation cell contained 108 000 atoms at a temperature of 500 K. Only Ni atoms are shown. This figure shows that most of the Ni atoms are segregated into one single cluster, consistent with the fact that Ag and Ni are immiscible at this temperature, where the estimated Ni solubility is much less than 0.2 at% at 500 K [35].

Figure 12(a) shows the same type of simulation starting with a pure fcc Ag bicrystal containing two $\Sigma 9$ (221) symmetric tilt GBs and doped by hybrid MC/MD technique with the target Ni concentration of 1 at% at 500 K. In this case, most Ni atoms segregate into only one of the two GBs, covering the boundary heterogeneously. This heterogeneous segregation behavior is characterized by the formation of two interfacial phases, with one phase rich of Ni atoms and the other almost Ni-free. When increasing the global composition to 2 at%, as shown in figure 12(b), one GB is fully covered with Ni atoms, while the other GB transforms into two interfacial phases. This heterogeneous segregation behavior is very similar to that of Au in Pt [84], but different from that of Cu in Ag. Figures 12(c) and (d) show the Cu segregation in this boundary simulated using the potential developed by Wu and Trinkle [56]. Cu atoms always distribute uniformly inside the two GBs, indicative of a typical homogeneous segregation.

Figure 13(a) demonstrates the Ni segregation in a Ag bicrystal containing two $\Sigma 11$ (113) symmetric $\langle 110 \rangle$ -tilt GBs. Contrary to the $\Sigma 9$ (221) GB, this type of GB has a low interface energy. Of all $\langle 110 \rangle$ symmetric tilt GBs, it only has higher energy than $\Sigma 3$ (111) coherent twin boundaries [79]. It is shown in this figure that Ni segregation behavior in this special boundary is different from its behavior in the $\Sigma 9$ (221) GB. Instead of forming two interfacial phases, Ni atoms tend to cluster inside one boundary. Increasing the global composition to 2 at% Ni does not change the clustering behavior, but only increases the cluster size, as shown in figure 13(b). In contrast, Cu in this GB type still shows a homogeneous segregation behavior, regardless of global composition, as shown in figures 13(c) and (d). Similarly, with 1 at% Ni segregation, our simulations predict that Ni atoms could form a cluster in an Ag bicrystal containing two coherent twin boundaries, each of which is attached with two (112) kink steps, as shown in figure 14(a). Interestingly, however, most Ni atoms tend to selectively

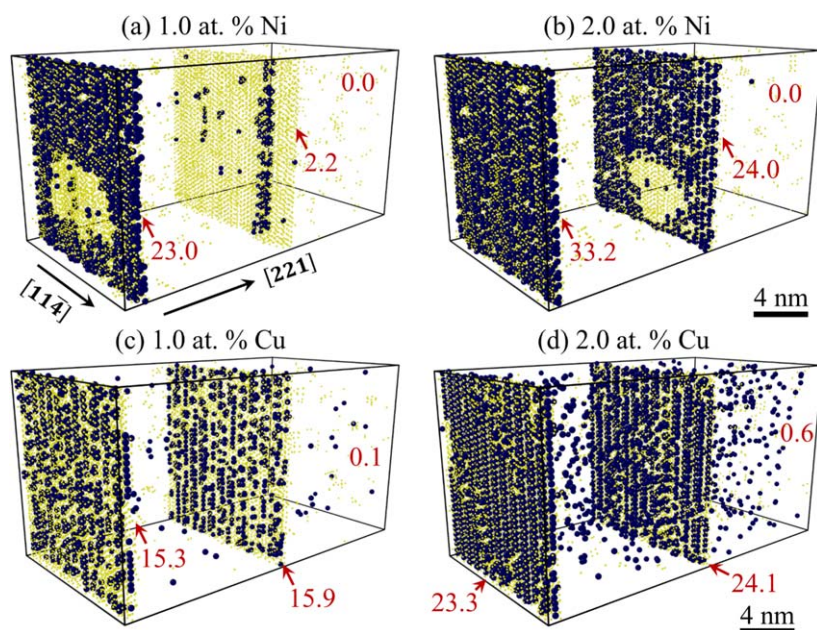


Figure 12. Heterogeneous Ni segregation versus homogeneous Cu segregation in high-energy $\Sigma 9$ (221) GBs at global compositions of (a), (c) 1 at% of solute atoms and (b), (d) 2 at% of solute atoms. All fcc-Ag atoms are omitted to enhance the view on the solute atom distribution, with the remaining Ag atoms colored in yellow. The local solute compositions (at%) in the grain interior and the two GBs are indicated in red color.

cluster along only one of the four kink steps. In sharp contrast, when the same structure is doped with 1 at% Cu, Cu atoms are uniformly segregated into all kink steps, as shown in figure 14(b).

With the Ag–Cu potential developed by Wu *et al* [56], atomistic simulations have shown that the segregation of Cu into nanotwinned Ag can change the incipient plasticity mechanism, resulting in a pronounced rise in yield strength [16]. The present simulations strongly suggest that Ni segregation into interface-strengthened Ag materials should substantially affect interface stability and mechanical behavior under stress and temperature, but through different mechanisms than Cu solutes, because Ni solute atoms have a distinctive segregation behavior, compared to that of Cu solutes, in both GBs and twin-boundary kink defects. Clearly, the new potential developed in this work could pave the way for such interesting studies.

4.2. GB amorphization behavior with high Ni contents

Figure 15 shows the equilibrium structure of a bicrystal model containing two $\Sigma 9$ (221) GBs when doped with a high Ni content, 10 at%. At high Ni concentration, the two interfaces become significantly disordered, transforming into two amorphous intergranular films. Interestingly, a close-up view of the GBs indicates that this amorphous film is not perfectly uniform. Ni atoms do not distribute randomly inside the film, as it should be for ideal amorphous phases, but rather preferentially form chain-like or cluster-like structures. This heterogeneous amorphous structure is consistent with the structure of an amorphous Ag–Ni

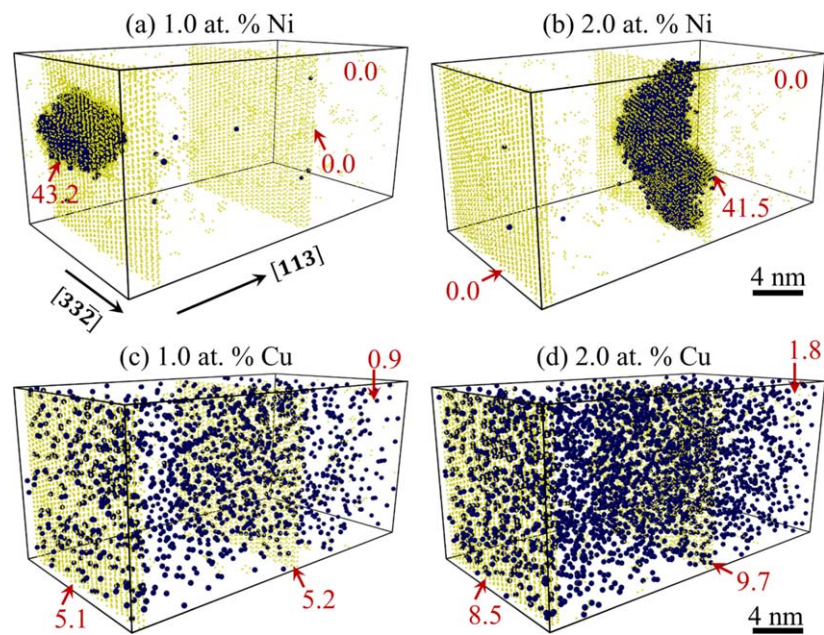


Figure 13. Ni clustering behavior versus homogeneous Cu segregation in low-energy $\Sigma 11$ (113) GBs at global compositions of (a), (c) 1 at% of solute atoms and (b), (d) 2 at% of solute atoms. All fcc-Ag atoms are omitted to enhance the view on the solute atom distribution, with the remaining Ag atoms colored in yellow. The local solute compositions (at%) in the grain interior, the two GBs, and the clusters formed inside are indicated in red color.

alloy fabricated experimentally by a vapor-quenching method [86]. This finding is important for several aspects. First, it proves that the new potential can successfully reproduce pervasive segregation-induced disordering transitions, and the complex phase transformations observed experimentally in the Ag GBs. Second, the formation of Ni-rich amorphous intergranular films could have direct ramifications for enhancing mechanical properties in crystalline Ag material. For example, it has been shown in the past that Cu–Zr amorphous films can efficiently reduce the damage induced by dislocation absorption at Cu GBs, holding great promise as fracture toughening mechanism for nanocrystalline Cu [32]. Likewise, Ni segregation induced amorphous films in Ag interfaces could offer new opportunities for designing tough materials, in addition to GB segregation strengthening mechanisms.

5. Conclusion

A semi-empirical FS potential suitable for the simulation of Ni solute segregation into Ag crystalline interfaces has been developed by fitting to a database derived from the *ab initio* calculations. The Ag–Ag interaction was optimized to correctly reproduce the stable and unstable stacking fault energies and liquid structure of pure Ag. The Ag–Ni cross potential was optimized to accurately predict the site-dependent Ni segregation energies in an Ag $\Sigma 9$ (221) GB, and the liquid structure of $\text{Ag}_{80}\text{Ni}_{20}$ alloys. This potential is shown to replicate with high fidelity not only properties at 0 K temperature included in the potential development procedure, but also those at elevated temperatures, such as transition states at interfaces.

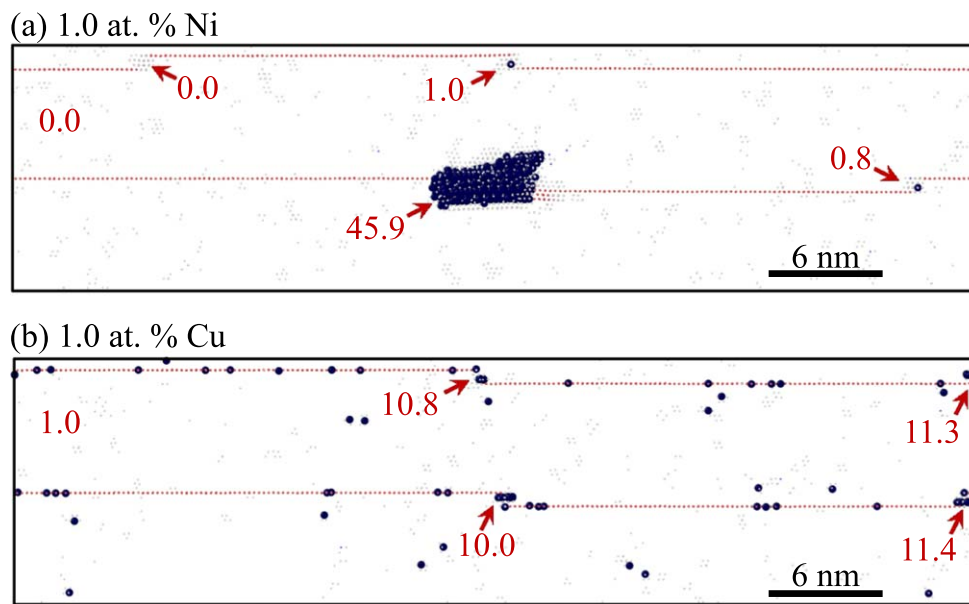


Figure 14. Ni clustering around twin-boundary defects. Atom segregation into $\Sigma 3(112)$ twin-boundary kink steps for (a) Ni solute and (b) Cu solute, at 1 at%. All fcc atoms are omitted to enhance the view on the solute atom distribution. The remaining Ag atoms are colored according to CNA, where the twin boundaries are identified by the red hcp atoms. Each twin-boundary kink step is indicated by a red arrow. The local solute compositions (at%) in the grain interior, the four kink steps, and the cluster formed in one of the kinks are indicated in red color.

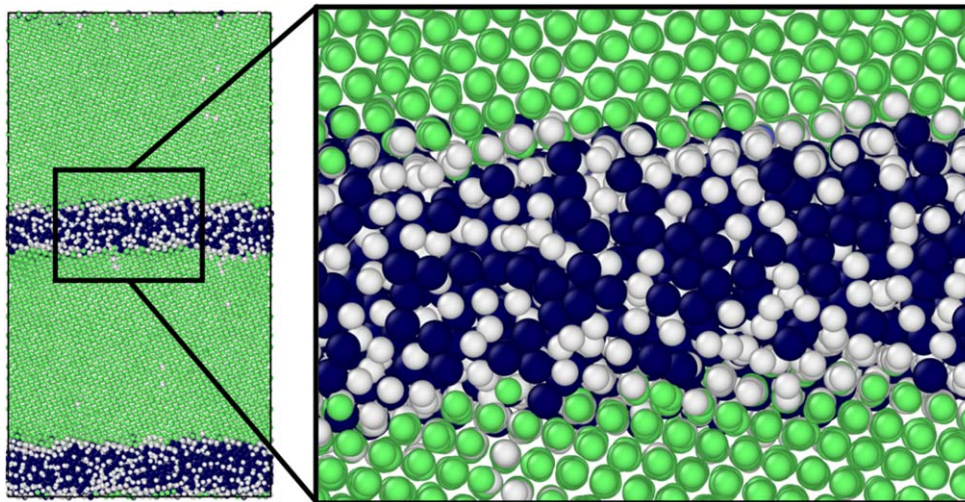


Figure 15. Ni segregation induced disordering transition at high Ni concentration (10 at%) in an fcc-Ag bicrystal containing two $\Sigma 9(221)$ symmetric tilt GBs, forming amorphous intergranular films with the heterogeneous structure shown in the close-up view of this film.


Hybrid MC/MD simulations with this potential show rich predictions leading to new understandings of atom segregation behavior at GBs. Using the new Ag–Ni potential with low Ni concentrations, our preliminary atomistic results on two different GB types, a high-energy $\Sigma 9(221)$ GB and a low-energy $\Sigma 11(113)$ GB, suggest that Ni segregation shows an interesting clustering phenomenon that is strongly dependent on the GB structure. This finding differs markedly from Cu-impurity segregation that is uniformly distributed along the interfaces. This selective Ni clustering behavior is also predicted for segregation to twin-boundary kink step imperfections. At higher Ni concentrations (10 at%), a GB transformation to amorphous intergranular films is found to prevail, which confirms experimental observations made in the past. Selective Ni segregation is potentially attractive as a fundamentally new mechanism of strengthening for interface-hardened Ag metals. It is therefore important that this segregation behavior can now be studied with this new Ag–Ni potential.

Acknowledgments

ZP and FS were supported for this work by US Department of Energy (DOE) under Grant No. DE-SC0016270. VB and MIM's research was supported by the US DOE, Office of Science, Basic Energy Sciences, Materials Science and Engineering Division and was performed at Ames Laboratory, which is operated for the US DOE by Iowa State University under Contract # DE-AC02-07CH11358. This research used resources of the National Energy Research Scientific Computing Center (NERSC), a US DOE Office of Science User Facility operated under Contract No. DE-AC02-05CH11231.

ORCID iDs

Zhiliang Pan  <https://orcid.org/0000-0003-3899-8761>

Frederic Sansoz  <https://orcid.org/0000-0002-2782-1832>

References

- [1] Seah M P and Hondros E D 1973 Grain boundary segregation *Proc. R. Soc. A* **335** 191
- [2] Westbrook J H and Wood D L 1961 Embrittlement of grain boundaries by equilibrium segregation *Nature* **192** 1280–1
- [3] Rice J R and Wang J-S 1989 Embrittlement of interfaces by solute segregation *Mater. Sci. Eng. A* **107** 23–40
- [4] Luo J, Cheng H, Asl K M, Kiely C J and Harmer M P 2011 The role of a bilayer interfacial phase on liquid metal embrittlement *Science* **333** 1730–3
- [5] Song J and Curtin W A 2013 Atomic mechanism and prediction of hydrogen embrittlement in iron *Nat. Mater.* **12** 145–51
- [6] Chookajorn T, Murdoch H A and Schuh C A 2012 Design of stable nanocrystalline alloys *Science* **337** 951–4
- [7] Murdoch H A and Schuh C A 2013 Stability of binary nanocrystalline alloys against grain growth and phase separation *Acta Mater.* **61** 2121–32
- [8] Hu J, Shi Y N, Sauvage X, Sha G and Lu K 2017 Grain boundary stability governs hardening and softening in extremely fine nanograined metals *Science* **355** 1292–6
- [9] Raabe D, Herbig M, Sandlöbes S, Li Y, Tytko D, Kuzmina M, Ponge D and Choi P P 2014 Grain boundary segregation engineering in metallic alloys: a pathway to the design of interfaces *Curr. Opin. Solid State Mater. Sci.* **18** 253–61
- [10] Pan Z and Rupert T J 2016 Effect of grain boundary character on segregation-induced structural transitions *Phys. Rev. B* **93** 134113

- [11] Cantwell P R, Tang M, Dillon S J, Luo J, Rohrer G S and Harmer M P 2014 Grain boundary complexions *Acta Mater.* **62** 1–48
- [12] Rupert T J 2016 The role of complexions in metallic nano-grain stability and deformation *Curr. Opin. Solid State Mater. Sci.* **20** 257–67
- [13] Dillon S J, Tai K and Chen S 2016 The importance of grain boundary complexions in affecting physical properties of polycrystals *Curr. Opin. Solid State Mater. Sci.* **20** 324–35
- [14] Hofmann S and Hofmann H 1985 Influence of grain boundary segregation on mechanical properties of activated sintered tungsten *J. Physique* **46** 633–40
- [15] Kameda J and McMahon C 1983 Solute segregation and hydrogen-induced intergranular fracture in an alloy steel *Metall. Mater. Trans. A* **14** 903–11
- [16] Ke X and Sansoz F 2017 Segregation-affected yielding and stability in nanotwinned silver by microalloying *Phys. Rev. Mater.* **1** 063604
- [17] Babicheva R I, Dmitriev S V, Bachurin D V, Srikanth N, Zhang Y, Kok S W and Zhou K 2017 Effect of grain boundary segregation of Co or Ti on cyclic deformation of aluminium bi-crystals *Int. J. Fatigue* **102** 270–81
- [18] Detor A J and Schuh C A 2007 Grain boundary segregation, chemical ordering and stability of nanocrystalline alloys: atomistic computer simulations in the Ni–W system *Acta Mater.* **55** 4221–32
- [19] Frolov T, Divinski S V, Asta M and Mishin Y 2013 Effect of interface phase transformations on diffusion and segregation in high-angle grain boundaries *Phys. Rev. Lett.* **110** 255502
- [20] Pan Z and Rupert T J 2017 Formation of ordered and disordered interfacial films in immiscible metal alloys *Scr. Mater.* **130** 91–5
- [21] Mendeleev M I, Srolovitz D J, Ackland G J and Han S 2005 Effect of Fe segregation on the migration of a non-symmetric $\Sigma 5$ tilt grain boundary in Al *J. Mater. Res.* **20** 208–18
- [22] Frolov T, Darling K A, Kecskes L J and Mishin Y 2012 Stabilization and strengthening of nanocrystalline copper by alloying with tantalum *Acta Mater.* **60** 2158–68
- [23] Subramanian P R and Perepezko J H 1993 The Ag–Cu (silver–copper) system *J. Phase Equilib.* **14** 62–75
- [24] Arias D and Abriata J P 1990 Cu–Zr (copper–zirconium) *Bull. Alloy Phase Diagr.* **11** 452–9
- [25] Subramanian P R and Laughlin D E 1989 The Cu–Ta (copper–tantalum) system *Bull. Alloy Phase Diagr.* **10** 652–5
- [26] Chakrabarti D J and Laughlin D E 1982 The Cu–Nb (copper–niobium) system *J. Phase Equilib.* **2** 455–60
- [27] Franke P and Neuschütz D 2006 *Binary Systems. Part 4: Binary Systems from Mn–Mo to Y–Zr: Phase Diagrams, Phase Transition: Data, Integral and Partial Quantities of Alloys* ed P Franke and D Neuschütz (Berlin: Springer) pp 1–3
- [28] Williams P L, Mishin Y and Hamilton J C 2006 An embedded-atom potential for the Cu–Ag system *Modelling Simul. Mater. Sci. Eng.* **14** 817
- [29] Mendeleev M I, Kramer M J, Ott R T, Sordelet D J, Yagodin D and Popel P 2009 Development of suitable interatomic potentials for simulation of liquid and amorphous Cu–Zr alloys *Phil. Mag.* **89** 967–87
- [30] Hashibon A, Lozovoi A Y, Mishin Y, Elsässer C and Gumbsch P 2008 Interatomic potential for the Cu–Ta system and its application to surface wetting and dewetting *Phys. Rev. B* **77** 094131
- [31] Zhang L, Martinez E, Caro A, Liu X-Y and Demkowicz M J 2013 Liquid-phase thermodynamics and structures in the Cu–Nb binary system *Modelling Simul. Mater. Sci. Eng.* **21** 025005
- [32] Pan Z and Rupert T J 2015 Amorphous intergranular films as toughening structural features *Acta Mater.* **89** 205–14
- [33] Khalajhedayati A, Pan Z and Rupert T J 2016 Manipulating the interfacial structure of nanomaterials to achieve a unique combination of strength and ductility *Nat. Commun.* **7** 10802
- [34] Borovikov V, Mendeleev M I and King A H 2018 Effects of Ag and Zr solutes on dislocation emission from $\Sigma 11(332)[110]$ symmetric tilt grain boundaries in Cu: bigger is not always better *Int. J. Plast.* **109** 79–87
- [35] Liu X J, Gao F, Wang C P and Ishida K 2008 Thermodynamic assessments of the Ag–Ni binary and Ag–Cu–Ni ternary systems *J. Electron. Mater.* **37** 210–7
- [36] Gas P, Poize S, Bernardini J and Cabane F 1989 A new approach to correlate grain boundary diffusion and segregation deduced from experimental measurements *Acta Metall.* **37** 17–24
- [37] Surholt T, Minkwitz C and Herzig C 1998 Nickel and selenium grain boundary solute diffusion and segregation in silver *Acta Mater.* **46** 1849–59

- [38] Mendelev M I, Kramer M J, Hao S G, Ho K M and Wang C Z 2012 Development of interatomic potentials appropriate for simulation of liquid and glass properties of NiZr₂ alloy *Phil. Mag.* **92** 4454–69
- [39] Becker C A, Tavazza F, Trautt Z T and de Macedo R A B 2013 Considerations for choosing and using force fields and interatomic potentials in materials science and engineering *Curr. Opin. Solid State Mater. Sci.* **17** 277–83
- [40] Kohn W and Sham L J 1965 Self-consistent equations including exchange and correlation effects *Phys. Rev.* **140** A1133–8
- [41] Perdew J P, Burke K and Ernzerhof M 1996 Generalized gradient approximation made simple *Phys. Rev. Lett.* **77** 3865–8
- [42] Perdew J P, Chevary J A, Vosko S H, Jackson K A, Pederson M R, Singh D J and Fiolhais C 1992 Atoms, molecules, solids, and surfaces: applications of the generalized gradient approximation for exchange and correlation *Phys. Rev. B* **46** 6671–87
- [43] Blöchl P E 1994 Projector augmented-wave method *Phys. Rev. B* **50** 17953–79
- [44] Kresse G and Joubert D 1999 From ultrasoft pseudopotentials to the projector augmented-wave method *Phys. Rev. B* **59** 1758–75
- [45] Plimpton S 1995 Fast parallel algorithms for short-range molecular dynamics *J. Comput. Phys.* **117** 1–19
- [46] Sadigh B, Erhart P, Stukowski A, Caro A, Martinez E and Zepeda-Ruiz L 2012 Scalable parallel Monte Carlo algorithm for atomistic simulations of precipitation in alloys *Phys. Rev. B* **85** 184203
- [47] Honeycutt J D and Andersen H C 1987 Molecular dynamics study of melting and freezing of small Lennard-Jones clusters *J. Phys. Chem.* **91** 4950–63
- [48] Stukowski A 2012 Structure identification methods for atomistic simulations of crystalline materials *Modelling Simul. Mater. Sci. Eng.* **20** 045021
- [49] Stukowski A 2010 Visualization and analysis of atomistic simulation data with OVITO—the open visualization tool *Modelling Simul. Mater. Sci. Eng.* **18** 015012
- [50] Finnis M W and Sinclair J E 1984 A simple empirical N-body potential for transition metals *Phil. Mag. A* **50** 45–55
- [51] Deng C and Sansoz F 2009 Fundamental differences in the plasticity of periodically twinned nanowires in Au, Ag, Al, Cu, Pb and Ni *Acta Mater.* **57** 6090–101
- [52] Jin Z H, Gumbsch P, Ma E, Albe K, Lu K, Hahn H and Gleiter H 2006 The interaction mechanism of screw dislocations with coherent twin boundaries in different face-centred cubic metals *Scr. Mater.* **54** 1163–8
- [53] Smith L and Farkas D 2018 Connecting interatomic potential characteristics with deformation response in FCC materials *Comput. Mater. Sci.* **147** 18–27
- [54] Borovikov V, Mendelev M I, King A H and LeSar R 2015 Effect of stacking fault energy on mechanism of plastic deformation in nanotwinned FCC metals *Modelling Simul. Mater. Sci. Eng.* **23** 055003
- [55] Borovikov V, Mendelev M I and King A H 2016 Effects of stable and unstable stacking fault energy on dislocation nucleation in nano-crystalline metals *Modelling Simul. Mater. Sci. Eng.* **24** 085017
- [56] Wu H H and Trinkle D R 2009 Cu/Ag EAM potential optimized for heteroepitaxial diffusion from *ab initio* data *Comput. Mater. Sci.* **47** 577–83
- [57] Zhou X W, Johnson R A and Wadley H N G 2004 Misfit-energy-increasing dislocations in vapor-deposited CoFe/NiFe multilayers *Phys. Rev. B* **69** 144113
- [58] Adams J B, Foiles S M and Wolfer W G 1989 Self-diffusion and impurity diffusion of fee metals using the five-frequency model and the embedded atom method *J. Mater. Res.* **4** 102–12
- [59] Ackland G J, Tichy G, Vitek V and Finnis M W 1987 Simple N-body potentials for the noble metals and nickel *Phil. Mag. A* **56** 735–56
- [60] Sheng H W, Kramer M J, Cadien A, Fujita T and Chen M W 2011 Highly optimized embedded-atom-method potentials for fourteen fcc metals *Phys. Rev. B* **83** 134118
- [61] Jin Z H, Dunham S T, Gleiter H, Hahn H and Gumbsch P 2011 A universal scaling of planar fault energy barriers in face-centered cubic metals *Scr. Mater.* **64** 605–8
- [62] Wu X-Z, Wang R, Wang S-F and Wei Q-Y 2010 *Ab initio* calculations of generalized-stacking-fault energy surfaces and surface energies for FCC metals *Appl. Surf. Sci.* **256** 6345–9
- [63] Li W, Lu S, Hu Q-M, Kwon S K, Johansson B and Vitos L 2014 Generalized stacking fault energies of alloys *J. Phys.: Condens. Matter* **26** 265005

- [64] Li R, Lu S, Kim D, Schönecker S, Zhao J, Kwon S K and Vitos L 2016 Stacking fault energy of face-centered cubic metals: thermodynamic and *ab initio* approaches *J. Phys.: Condens. Matter* **28** 395001
- [65] Kibey S, Liu J B, Johnson D D and Sehitoglu H 2007 Predicting twinning stress in fcc metals: linking twin-energy pathways to twin nucleation *Acta Mater.* **55** 6843–51
- [66] Suzuki H and Barrett C S 1958 Deformation twinning in silver–gold alloys *Acta Metall.* **6** 156–65
- [67] Tian F-Y, Chen N-X, Shen J and Vitos L 2012 A novel potential: the interlayer potential for the fcc (111) plane family *J. Phys.: Condens. Matter* **24** 045001
- [68] Hartford J, von Sydow B, Wahnström G and Lundqvist B I 1998 Peierls barriers and stresses for edge dislocations in Pd and Al calculated from first principles *Phys. Rev. B* **58** 2487–96
- [69] Rosengaard N M and Skriver H L 1993 Calculated stacking-fault energies of elemental metals *Phys. Rev. B* **47** 12865–73
- [70] Schweizer S, Elsässer C, Hummler K and Fähnle M 1992 *Ab initio* calculation of stacking-fault energies in noble metals *Phys. Rev. B* **46** 14270–3
- [71] Kioussis N, Herbranson M, Collins E and Eberhart M E 2002 Topology of electronic charge density and energetics of planar faults in fcc metals *Phys. Rev. Lett.* **88** 125501
- [72] Efimov A I, Belorukova L P, Vasilkova I V and Chechev V P 1983 *Svoistva Neorganicheskikh Soedinenii. Spravochnik* (Leningrad: Himija)
- [73] Van Swygenhoven H, Derlet P M and Frøseth A G 2004 Stacking fault energies and slip in nanocrystalline metals *Nat. Mater.* **3** 399–403
- [74] Zimmerman J A, Gao H J and Abraham F F 2000 Generalized stacking fault energies for embedded atom FCC metals *Modelling Simul. Mater. Sci. Eng.* **8** 103–15
- [75] Lu N, Du K, Lu L and Ye H Q 2015 Transition of dislocation nucleation induced by local stress concentration in nanotwinned copper *Nat. Commun.* **6** 7648
- [76] Bufford D, Wang H and Zhang X 2011 High strength, epitaxial nanotwinned Ag films *Acta Mater.* **59** 93–101
- [77] Furnish T A and Hodge A M 2014 On the mechanical performance and deformation of nanotwinned Ag *APL Mater.* **2** 046112
- [78] Ott R T, Geng J, Besser M F, Kramer M J, Wang Y M, Park E S, LeSar R and King A H 2015 Optimization of strength and ductility in nanotwinned ultra-fine grained Ag: twin density and grain orientations *Acta Mater.* **96** 378–89
- [79] Sansoz F and Molinari J F 2005 Mechanical behavior of Σ tilt grain boundaries in nanoscale Cu and Al: a quasicontinuum study *Acta Mater.* **53** 1931–44
- [80] Sansoz F and Molinari J F 2004 Incidence of atom shuffling on the shear and decohesion behavior of a symmetric tilt grain boundary in copper *Scr. Mater.* **50** 1283–8
- [81] Wang Y M, Sansoz F, LaGrange T, Ott R T, Marian J, Barbee T W Jr and Hamza A V 2013 Defective twin boundaries in nanotwinned metals *Nat. Mater.* **12** 697–702
- [82] Fang Q and Sansoz F 2017 Influence of intrinsic kink-like defects on screw dislocation—coherent twin boundary interactions in copper *Acta Mater.* **123** 383–93
- [83] Mendeleev M I and Srolovitz D J 2002 Determination of alloy interatomic potentials from liquid-state diffraction data *Phys. Rev. B* **66** 014205
- [84] O'Brien C J, Barr C M, Price P M, Hattar K and Foiles S M 2018 Grain boundary phase transformations in PtAu and relevance to thermal stabilization of bulk nanocrystalline metals *J. Mater. Sci.* **53** 2911–27
- [85] Minkwitz C, Herzig C, Straumal B B and Gust W 1998 Radiotracer diffusion of Ni and Ag in Ag and Ni grain boundaries and oriented Ag/Ni interphase boundaries *Mater. Sci. Forum* **294–296** 541–4
- [86] He J H, Sheng H W, Schilling P J, Chien C L and Ma E 2001 Amorphous structures in the immiscible Ag–Ni system *Phys. Rev. Lett.* **86** 2826–9